HAL
open science

# Numerical investigation of bend and torus flows-Part II : Flow simulation in torus reactor

Jeremy Pruvost, J. Legrand, P. Legentilhomme, J.M. M Rosant

## To cite this version:

Jeremy Pruvost, J. Legrand, P. Legentilhomme, J.M. M Rosant. Numerical investigation of bend and torus flows-Part II : Flow simulation in torus reactor. Chemical Engineering Science, 2004, 59 (16), pp.3359-3370. 10.1016/j.ces.2004.03.041 . hal-02534038

**HAL Id: hal-02534038**

**https://hal.science/hal-02534038v1**

Submitted on 17 Apr 2020

**HAL** is a multi-disciplinary open access archive for the deposit and dissemination of scientific research documents, whether they are published or not. The documents may come from teaching and research institutions in France or abroad, or from public or private research centers.

L'archive ouverte pluridisciplinaire **HAL**, est destinée au dépôt et à la diffusion de documents scientifiques de niveau recherche, publiés ou non, émanant des établissements d'enseignement et de recherche français ou étrangers, des laboratoires publics ou privés.

# Numerical investigation of bend and torus flows—Part II : Flow simulation in torus reactor

J. Pruvost[a,*], J. Legrand[a], P. Legentilhomme[a], J.M. Rosant[b]

[a] *Faculté des Sciences et des Techniques, University of Nantes, GEPEA Laboratory, UMR-CNRS 6144, 2, rue de la Houssinière, BP 92208, 44322 Nantes Cedex 3, France*

[b] *Fluid Mechanics Laboratory, UMR-CNRS 6598, Ecole Centrale de Nantes, BP92101, 44321 Nantes Cedex 3, France*

**Abstract**

Flow in a torus reactor with straight parts fitted with a marine impeller is investigated. The laser Doppler anemometry (LDA) is first employed to achieve experimental measurements of mean velocity profiles. Next, a numerical resolution of the steady-state flow is performed using a multiple reference frames (MRF) approach to represent the particular flow induced by the marine impeller in the geometry. A comparison of predictions using different turbulence models to LDA measurements is made, and a $k$–$\omega$ model is assessed.

The numerical tool is used to investigate in more details the particular flow induced in the torus geometry. Evolution of the axial and rotating motions when moving away from the impeller is especially investigated, showing the complex hydrodynamical interaction between the main rotating swirl motion involved downstream the impeller, and bend curvature effects. Two different flow conditions can be considered in the torus geometry, with a main swirling motion close to the impeller, which freely decays and vanishes when Dean vortices appear in bends. Simulations for two rotation velocities of the impeller and comparison with the study with simple bends (first part) reveal pertinence of the swirl number $Sn$ to describe the change of flow conditions along the reactor axis. When this parameter decreases below a threshold value around 0.2 in a bend entry, centrifugal effects due to bend curvature are more important than the swirl motion, and Dean vortices appear in bend outlet. One main consequence is the axial distance of the swirl motion persistence, which is found to be smaller for the higher impeller rotation velocity, due to the dual effect of the marine impeller that generates simultaneously both axial and rotating motions.

*Keywords:* Hydrodynamics; Torus reactor; Simulation; Numerical analysis; Swirling flow; Turbulence

## 1. Introduction

Torus reactors could be more interesting than classical stirred tanks in some chemical engineering applications (Legrand and Belleville, 2002; Belleville et al., 1992; Nouri et al., 1997). The loop configuration involves low-pressure drop, and thus reduces power consumption for a given mixing operation (Legrand and Belleville, 2002). Another advantage is the high dispersion achieved because of Dean vortices involved by the reactor bends, and of the use of a marine screw impeller in the torus axis that generates an efficient three-dimensional swirling motion in the geometry. The combination of these two effects leads to an absence of dead volumes in the reactor, that facilitates the scaling-up of its performance. Residence time can be very accurately controlled, making torus reactors very interesting for biochemical applications like enzymatic reactions (Legrand et al., 1997; Nouri et al., 1997), or heterogeneous liquid–liquid reaction (Tanaka and O'Shima, 1988).

But, despite the efficiency of such geometry, few information about hydrodynamical characteristics involved in torus shape reactors are known. Khalid et al. (1996) and Khalid and Legrand (2001) emphasize the main features of the flow, and especially the high degree of mixing and the decay of the swirl motion when moving far from the marine impeller. Other studies are mainly restricted to global measurements, like the circulation time as a function of the impeller rotation (Sato et al., 1979), or general overview of the flow

structure using tracers methods (Legrand and Belleville, 2002). This is mainly explained by the difficulties encountered to conduct an experimental investigation of this complex flow. For example, probes measurement techniques, like hot-wire, are especially sensible to the flow direction, making their use in swirling flow, and so in torus reactors, ambiguous. In the same way, bends, and especially wall curvature, make it difficult for the use of non-intrusive optical measurements, such as particle image velocimetry (PIV) or laser Doppler anemometry (LDA). The involved optical distortions request particular acquisition procedure, and possible data post-correction. In this purpose, computational fluid dynamics (CFD) appears as an interesting tool, because various hydrodynamical characteristics can be accessed in the entire geometry. The modelling of the entire flow in torus reactor is however not easy, because of the combined effects of the bend curvature and the impeller. As shown in the first part of this study, interaction between the helical motion with Dean vortices can be strong, but numerical simulation predicts with accuracy the resulting flow in bend outlet. The choice of the turbulence model was shown to be important but, despite turbulence is known to be anisotropic in bends (Sudo et al., 1998; Anwer and So, 1993), simple models, based on association of standard wall-functions with $k-\varepsilon$ turbulence models, were revealed to be sufficient. Only a slight improvement was observed in the case of inlet swirl motion, with the use of a low-$Re$ $k-\varepsilon$ model involving a full resolution of the boundary layer.

In this study, numerical investigation is extended to the case of the torus reactor geometry, using the commercial code FLUENT. From an engineering point of view, such a solver is sufficiently accurate and can be employed as a "black box" numerical tool in process investigation, by especially giving complementary informations to experimental characterization (Brucato et al., 1998; Yoon et al., 2001). Numerical modelling necessitates the simulation of flow generated by rotating marine impellers. Many examples are available in the literature, in various research topics including mixing problems in stirred tanks (Yoon et al., 2001; Revstedt et al., 1998; Brucato et al., 1998), or pilot plants (Harris et al., 1996; Ten Cate et al., 2001). Different numerical solutions can be retained, depending on the geometry to be modelled and available informations (Brucato et al., 1998; Harris et al., 1996). The simple one, called the fixed-velocity or velocity data method, substitutes the impeller by boundary velocities generated in its vicinity, that allows the impeller not to be modelled. But this implies to experimentally measure those velocities (Yoon et al., 2001; Bali, 1998), or to make some assumptions in the flow generated (Revstedt et al., 1998; Pericleous and Patel, 1987). The second method is the modelling of the impeller, by using for example a rotating frame to simulate the impeller rotation (Brucato et al., 1998). Such an approach was retained in this study and validated by comparison to experimental measurements. The last part of the study is devoted to a numerical analysis of the particular flow conditions involved in the torus reactor, and especially the competition between the swirl motion, due to the impeller rotation, with Dean vortices generated by bends.

## 2. Torus reactor description

The torus reactor investigated is described in Khalid and Legrand (2001). This reactor having a volume of 9.2 l was especially designed with straight lengths to facilitate experimental investigation. It consists of four 90° bends having curvature radius $R_c$ equal to 0.315 m, each bend being connected with straight tubes of 0.15 m in length. The reactor has a constant circular cross-section with a inner tube diameter $D = 0.067$ m. The total length $L$ of the reactor is 2.45 m. The reactor is transparently constructed, so as to allow experimental characterization using optical measurements.

Flow is induced by a marine-type impeller with three blades. The impeller diameter is $d_1 = 0.053$ m with an axis diameter $d_2 = 0.012$ m. The blade pitch $\phi$ is 45°. The impeller is set in one of the straight lengths. For convenience, bends and straight lengths are numbered, and inner and outer part of the torus geometry are defined as in Fig. 1. Khalid et al. (1996) used a geometrical parameter $F_g$ to relate the dimensions of the marine impeller and the torus reactor:

$$F_g = \frac{d_1^2 - d_2^2}{D^2}\, tg\phi. \tag{1}$$

In this case, $F_g$ is constant and equal to 0.594. The impeller rotational velocity, $N$, is ranged between 200 and 2000 rpm, and is measured using a tachometer. Experimentations were carried with water at ambient temperature.

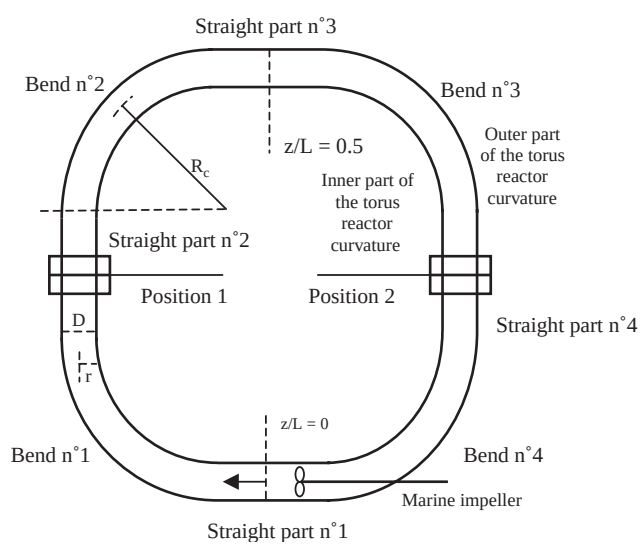


Fig. 1. Schematic representation of the torus reactor.

## 3. Experimental investigation

Khalid et al. (1996) and Khalid and Legrand (2001) have already made an experimental investigation of the torus reactor by using electrochemical probes. But the electrochemical probe gives only rough approximations of velocities values. In this study, to validate the flow computation, another experimental investigation was conducted using the LDA technique, that allows more accurate velocity measurements.

The LDA technique is a well-established non-intrusive optical technique. The system used in this study is commercially available by Dantec. It consists of a continuous laser source (argon-type with emitting power of 2 W), transmitting optics (beam splitter and focusing lens) and receiving optics (photodetectors PM55X08 and PM57X08). The beam splitter is used to generate three laser beams of different wavelengths that permit simultaneous acquisition of two velocity components. In order to distinguish between positive and negative flow direction, an acoustic-optical modulator (Bragg cell) is used. Iodine particles with size of a few micrometers were used as tracer.

As discussed before, the problem in torus geometry is the optical distortion that results from the curvature of pipe and bends associated to the difference in optical index between water and air. This explains the choice of straight lengths in the torus geometry, which were made in a square-sectioned transparent box (Fig. 1). The only remaining curved interface is due to the inner wall of the reactor. To allow LDA measurements, a small correction of initial beams positions was thus applied to make beams intersect. The position correction was determined using standard optical theories.

LDA technique was employed to measure axial and circumferential components of mean velocities along an horizontal diameter located at the center of the second and fourth straight parts, respectively named positions 1 and 2 (Fig. 1). These locations were retained to investigate the flow behavior after the first bend outlet, and its evolution far away from the impeller, after the third bend. Measurements were achieved for four impeller rotation speeds, $N = 500, 900, 1600$ and 1985 rpm, that correspond respectively to Reynolds numbers, $Re = 19900, 35800, 63670, 79000$.

## 4. Description of the numerical method

### 4.1. Grid consideration

The torus reactor is three-dimensionally meshed using the GAMBIT software (Fluent Inc.). The resulting grid is shown in Fig. 2. Due to the impeller, a regular mesh is difficult to apply in the entire geometry. A hybrid mesh was thus retained, with an irregular zone composed of tetrahedral volumes and prisms in the first straight part corresponding to the marine impeller location, and a regular mesh with elementary hexahedral volumes in the remaining parts.

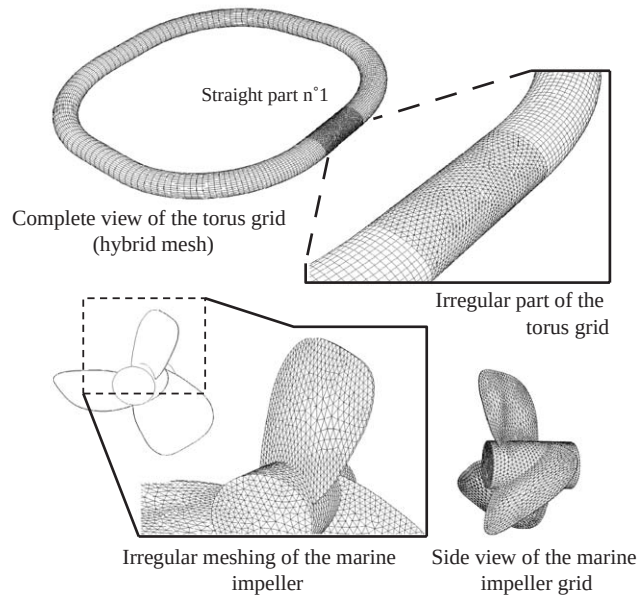


Fig. 2. Mesh topology.

The regular parts are meshed as single bends described in the first part of the study, with two zones for a given cross-section. The near-wall region mesh is structured, while an unstructured grid is employed in the bulk region. The grid discretization in the circumferential direction is uniform, but the radial distribution is chosen in order to increase the number of elementary volumes when getting close to the walls. In the axial direction, a constant discretization is retained except for bends 1 and 4, where the cells density is refined as going closer to the first straight part with an irregular mesh that involves small cells. By this way, a very large difference in cell volume between adjacent cells is avoided.

To generate the grid of the irregular part, the impeller surface and the outer tube wall are first meshed. A refinement function (named size function in FLUENT) is next applied in the vicinity of tube and impeller walls to control the cells density in boundary layers. This function fixes the size of the first near-wall elementary volume and the discretization step. The size of the first cell was chosen with respect to the two different near-wall considerations tested in the study, the first being a standard approach, with application of a wall-function based on the universal logarithmic profile (standard wall-function), and the second a full resolution of momentum equations in the boundary layer using a Low-*Re* model. The criterion $y^+$ was used to characterize the first cell location in wall-coordinate:

$$y^+ = \frac{\rho u_\tau y}{\mu}, \tag{2}$$

where $u_\tau$ is the wall-friction velocity, $y$, the normal distance from the center of the cell to the wall, $\rho$ the fluid density and $\mu$ the fluid viscosity.

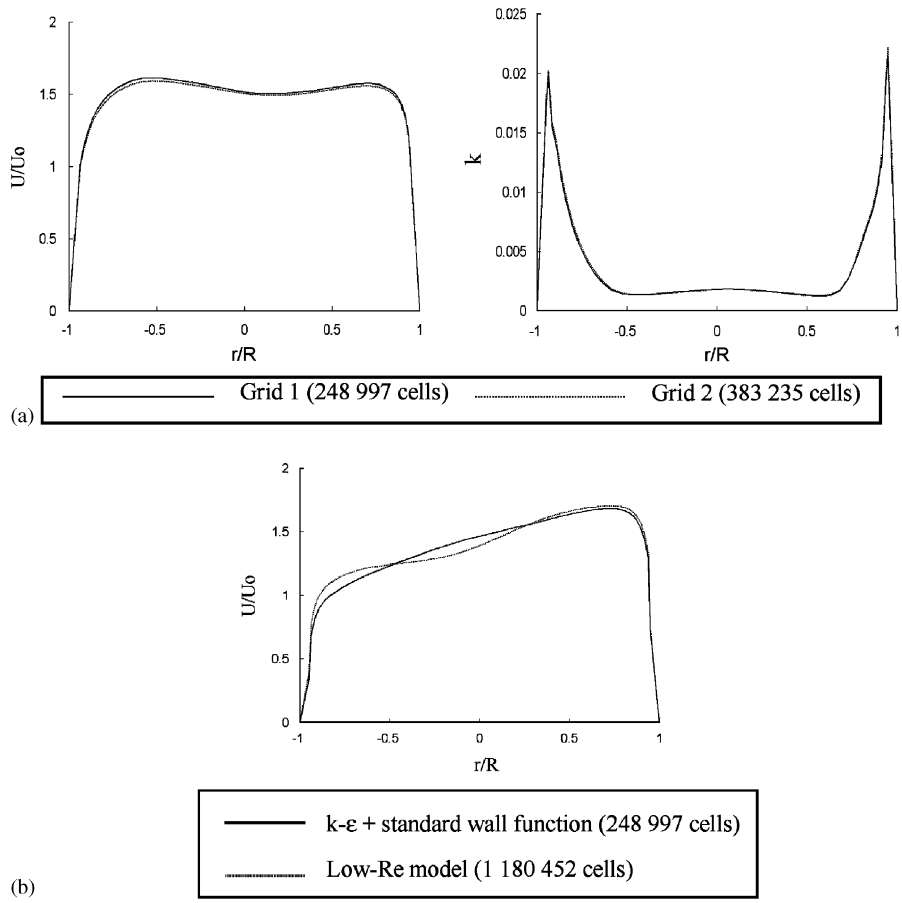


Fig. 3. Grid definition: (a) influence of the grid refinement using $k$–$\varepsilon$ model with standard wall-function on mean axial velocity and turbulent energy profile in position 1; (b) influence of the boundary layer consideration on mean axial velocity profile in position 2.

When the logarithmic law is employed, $y^+$ has to be close to $y^+ = 30$ and, for the full boundary layer resolution, close to $y^+ = 1$, with at least 10 cells in the boundary layer. The drawback of the boundary layer resolution is the very fine grid required by this method, as already discussed for curved ducts in the first part of the study.

Various preliminary trials were made to estimate adequate grid characteristics, and especially to follow the near-wall constraints after convergence. A grid with 248997 cells was defined (Grid 1). Grid independency of the results was verified by varying mesh parameters so as to refine topology, and by comparing two values, the mean axial velocity $U$ and the turbulent kinetic energy $k$ profiles obtained at position 1. Results of Fig. 3a obtained with a fine mesh having 383 235 cells show the independency of the grid using mesh discretization for the wall-function approach ($y^+ = 30$).

But, because of the bend curvature and swirl motion, the boundary layer can be disturbed, and thus the universal logarithmic law cannot be verified. However, simulations achieved using the universal logarithmic law approximation revealed to be sufficient in most cases, due to the robustness of the method. This was especially observed with swirling flows applied in simple bends, where only a slight improvement was obtained with a full resolution of the boundary layer. Nevertheless, in order to investigate the interest of such an approach for the torus geometry, a Low-*Re* model is tested, with a very fine refinement applied near the walls. Results of axial velocity profiles predicted in position 2 are given in Fig. 3b for the normal mesh (Grid 1) with a $k$–$\varepsilon$ model associated to the standard wall function, and for a very fine one with 1 180 452 cells to allow a full resolution of the boundary layer using the low-*Re* model. The slight difference shows that the increase in grid size is not necessary, comparison leading to almost the same results but with greater computation time. Grid 1 was thus retained for the study.

### 4.2. Turbulence models and numerical details

A review of the literature on turbulence models efficiency for bend and swirl flow modelling was made in the first part of this study. In the torus reactor, because of the impeller, the flow behavior is different, and the modelling approach had thus to be especially investigated. Various models were thus tested, two of eddy-viscosity type, namely the standard

$k$–$\varepsilon$ model and the $k$–$\omega$ model, and one Reynolds-stress model. Those models are described in the literature (Wilcox, 1998), and the standard $k$–$\varepsilon$ and $k$–$\omega$ models, and the Reynolds-stress were already tested for the single bend case.

As in part I, various preliminary trials were made to determine best configuration for each turbulence model. A second-order interpolation scheme was applied for pressure and velocity interpolation, and a power-law interpolation for turbulent characteristics revealed to give best results for all approaches. The pressure–velocity coupling was solved using the iterative correction procedure "SIMPLEC". Computations were performed until convergence of all the residual criteria was found (no variation). For all simulations, default constants of the turbulent models retained in FLUENT were employed and a steady-state calculation was made.

### 4.3. Boundary conditions and numerical details

The torus reactor is of closed type, and thus no inlet or outlet flow conditions are applied. The flow results from the impeller rotation which is the only driving mechanism. In the case of such moving parts in geometries, two principal modelling solutions are employed, depending on the complexity of the problem. These solutions are the multiple reference frames (MRF), and the sliding mesh (SM) approaches. The MRF method, which is the simplest one, reveals to be sufficient in this study, and was thus retained. In the SM approach, the geometry grid is divided in two parts, one being stationary, and the other one being associated with the rotating part. The two grids then slide past each other in a time-dependent manner. The flow-field is thus solved in its unsteady state, that allows an accurate representation of the interactions between moving and stationary parts, but in counterparts, is more computer time consuming (Montane et al., 2001). This approach has thus to be retained only when those interactions are strong, or when a transient investigation is desired. With the MRF approach, a steady-state solution is achieved by solving the equations of motion in different reference frames, one being the absolute inertial frame, others being in rotation and attached to impellers (Brucato et al., 1998). In the torus case, a rotating frame is linked to the impeller with a rotation velocity $\Omega$ equal to that of the impeller. The surrounding flow (in the straight part no 1) is then solved in this rotating frame, while standard resolutions are performed in the remaining parts of the reactor, which are stationary in the absolute inertial frame. A relation between the equations in moving and stationary parts is deduced from the decomposition of absolute velocity in the rotating frame:

$$\vec{v}_r = \vec{v} - \Omega\vec{\mathbf{r}}, \tag{3}$$

where $\vec{v}_r$ is the relative velocity vector in the rotating frame, $\vec{v}$ the absolute one, and $\vec{\mathbf{r}}$ is the position vector in the rotating frame.

Using this formulation, momentum equations are, in the case of a steady-state flow:

in the absolute reference frame, with $p$, the pressure,

$$\nabla \cdot (\rho\vec{v}\vec{v}) = -\nabla p + \nabla \cdot (\vec{\tau} + \vec{\tau}') \tag{4}$$

in the relative rotating reference frame,

$$\nabla \cdot (\rho\vec{v}_r\vec{v}_r) + \rho(2\vec{\Omega}\vec{v}_r + \vec{\Omega}\vec{\Omega}\vec{\mathbf{r}}) = -\nabla p + \nabla \cdot (\vec{\tau} + \vec{\tau}') \tag{5}$$

with $\vec{\tau}$ the molecular stress-tensor,

$$\vec{\tau} = -pI + \mu(\nabla\vec{v} + (\nabla\vec{v})^{\mathrm{T}}) \tag{6}$$

and $\vec{\tau}'$ the turbulent stress-tensor,

$$\vec{\tau}' = -\rho\overline{v'v'}. \tag{7}$$

The introduction of the relative velocity in the momentum equations adds additional terms to the classical absolute reference frame formulation. Those terms express the increase of the fluid acceleration due to the rotating motion. By solving those equations in corresponding parts of the geometry and using Eq. (3) to relate the results, the entire steady-state flow including impeller rotation effect is finally obtained.

Because of the loop configuration of the reactor, convergence is difficult to achieve. Indeed, with MRF resolution, the only boundary condition to be specified is the rotation velocity of the impeller. The flow generated by the impeller itself has thus to be correctly solved as well as the one in the remaining part of the reactor, both having strong interactions. In order to facilitate the convergence to the steady-state flow, the rotational velocity of the impeller was increased in two or three successive steps, depending of convergence difficulties. Intermediate converged solutions were used to initialize hydrodynamical values for the next higher rotation velocity.

## 5. Numerical results

### 5.1. Validation

To investigate if the mean bulk velocity in the torus reactor was accurately predicted using MRF approach, a first global validation was made by simulating flows as a function of the impeller rotation velocity with the $k$–$\varepsilon$ model, and results were compared to the correlation experimentally determined by Belleville et al. (1992) and used by Khalid et al. (1996):

$$U_0 = 0.06F_gN, \tag{8}$$

where $U_0$ is the mean bulk velocity, $N$, the rotation velocity of the impeller. $F_g$ is defined in Eq. (1).

This correlation specifies a proportionality between the impeller rotation speed and the resulting mean bulk velocity. Khalid et al. (1996) have estimated the correlation accuracy, which is equal to about 10% up to $N = 800$ rpm, and 20% for higher values of the rotation speed. Results in Fig. 4 are thus in agreement with this correlation, confirming

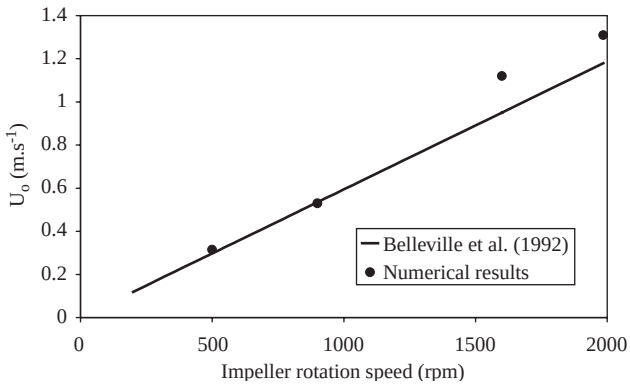


Fig. 4. Mean bulk velocity as a function of the impeller rotation speed: comparison with the empirical correlation of Belleville et al. (1992).

the choice of the MRF method for the impeller modelling. As observed experimentally, errors increase with the rotation velocity, but remain in an acceptable range, considering the accuracy of the correlation.

Influence of the turbulence modelling has been investigated next for two impeller rotation speeds, namely $N_1 = 900$ rpm and $N_2 = 1985$ rpm. Validation was made with comparison to experimental LDA measurements, as shown in Fig. 5a for $N_1$, and in Fig. 5b for $N_2$. Predicted mean profiles are given for positions 1 and 2 for the axial component, and position 1 for the circumferential component. As depicted in Fig. 5, the order of magnitude of velocities is well-predicted, whatever the model. For the axial component at position 1, a flat-type profile is observed, with a slight over-estimation. For position 2, a shift of the maximum of the velocity toward the outer part (i.e. $r/R > 0$) of the torus curvature is predicted, but this shift is not experimentally so pronounced. For the circumferential component, results show the good prediction of the increase of the swirl motion with the impeller rotation speed. No significant difference is observed when comparing turbulent models influence on this component, in contrary to the results on the axial component. By comparing predictions of the axial component for $N_1$ (Fig. 5a), it is difficult to conclude about the turbulence models effectiveness. The $k$–$\omega$ model seems to give better predictions in position 1, but not in position 2. For this last position, it appears that the standard version of the $k$–$\varepsilon$ model is in contrary more effective for the inner part (i.e. $r/R < 0$), but not for the outer one. No conclusion can thus be made at this stage of the validation. Main features of the flow involved in the torus reactor are well represented by each model, but none of them revealed better prediction. Only RSM seems to give less accurate results, like observed for the bend flows in part I of the study. For the higher rotation velocity of the impeller $N_2 = 1985$ rpm, the over-prediction of axial velocity is still observed at position 1, except for the $k$–$\omega$ model that leads to more accurate prediction. The same tendency is noticed for position 2, with better results for the $k$–$\omega$ model especially for the outer part of the curvature. But comparison with the experimental profile shape is not fulfilled, even for the $k$–$\omega$ model. For position 1, predictions conclude that the

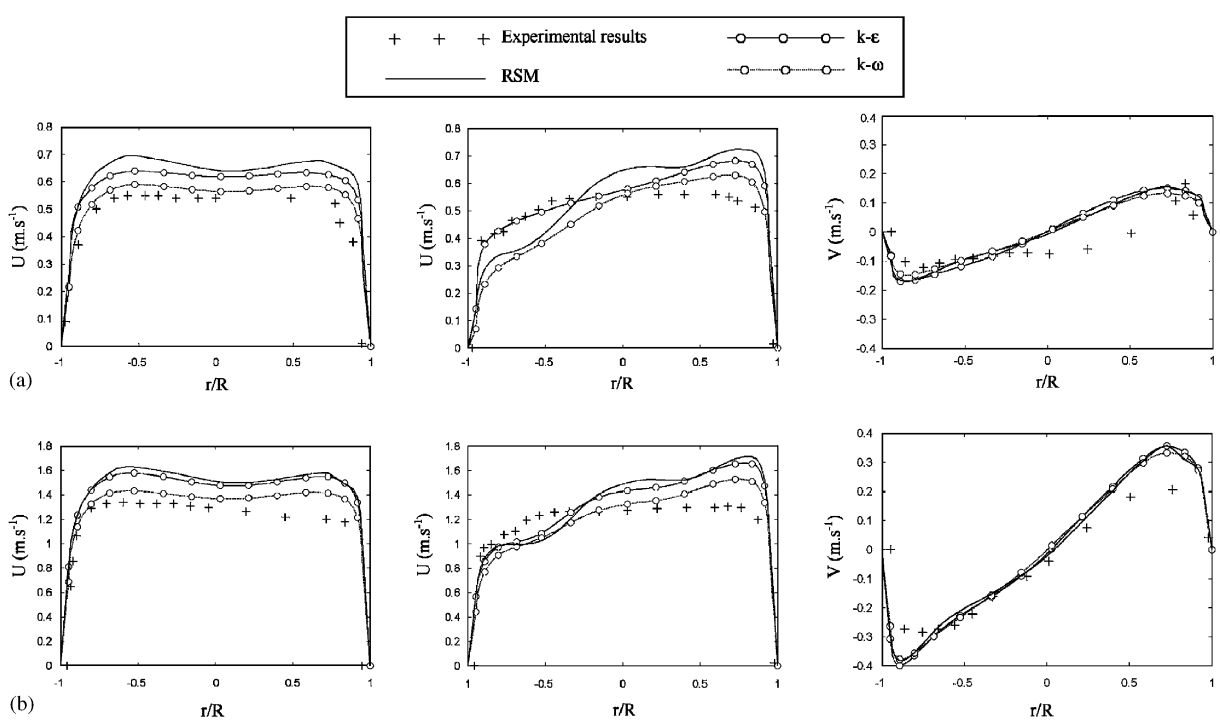


Fig. 5. Numerical predictions for different numerical models for mean axial velocity in position 1 (left) and position 2 (right), and for the circumferential velocity in position 1 (bottom). (a) for $N_1 = 900$ rpm; (b) for $N_2 = 1985$ rpm.

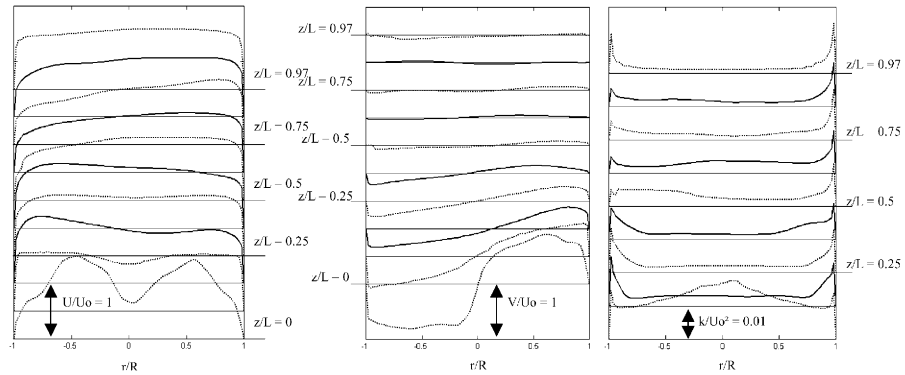


Fig. 6. Longitudinal evolutions of predicted velocity profiles for $N_2 = 1985$ rpm (left: axial component; center: circumferential component; right: turbulent kinetic energy).

axisymmetry of the axial velocity profiles next to the first bend, whereas experimental measurements reveal a slight increase in the inner part of the torus reactor. However, this small difference can be explained by the experimental uncertainty which is around 10%. In position 2, the difference between the predicted and experimental values is bigger, especially when going closer to the walls. Because of the decrease in accuracy of LDA measurements in this region, due to difficulties in positioning beams to make them correctly intersect near the walls, it is again difficult to conclude, but it seems that no accurate prediction can be achieved in this region. This is certainly explained by the use of the log-law based wall-function that induces a loss of accuracy near the walls, as observed for curved bends. The maximum deviation between experimental and predicted values does not exceed 20% of the mean bulk velocity. Prediction of the circumferential velocity is less accurate, but it must be noticed that its measurement is more difficult to experimentally conduct than the axial component, especially for low impeller rotation speed as for $N_1$, a poor swirl motion being generated, even in position 1. It can then be concluded that the $k$–$\omega$ model allows a relative accurate estimation of the flow involved in the torus reactor. This model will be thus employed in the next part for a detailed investigation of the flow.

### 5.2. Numerical characterization of the flow in the torus reactor

Evolutions of predicted mean axial and circumferential components of velocity profiles, and turbulent kinetic energy profiles are presented in Fig. 6 for $N_2 = 1985$ rpm. To visualize the particular behavior of the axial component, those corresponding values are plotted on a schematic representation of the torus reactor geometry in Fig. 7. Fig. 6 shows the flow conditions involved just downstream of the impeller, with a high turbulent and swirl intensity, and an axisymmetric profile of the axial component with two maxima near the walls, and low values behind the impeller axis. For downstream positions, this feature vanishes with the fast decay of the swirl motion. The decrease of the turbulent kinetic energy shows the impeller effect on the turbulence generation, and thus turbulent mixing. For a position just behind the impeller, the maximum of turbulent kinetic energy is located at the center of the pipe section. Downstream the impeller, maxima are located near walls, as observed in part I. If the first bend is considered, an interesting characteristic of the flow in torus reactor is observed. The maximum of axial velocity is located in the inner part of the bend, contrary to common bend flows where it is well known that the centrifugal effects tend to shift the maximum of velocity towards the outer part. In the first part of this study, even in the case when a solid body rotation was applied in the single bend entry, only a decrease of the value of the maximum velocity was observed in the outlet section for highest values of swirl intensities, but never a shift from the outer part to the inner one. For the torus reactor, by using an electrochemical

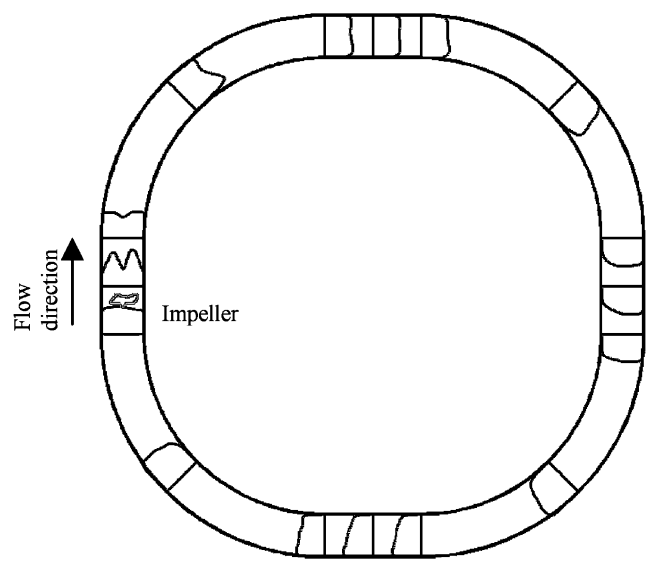


Fig. 7. Evolution of the shape of mean axial velocity profiles in the torus geometry.

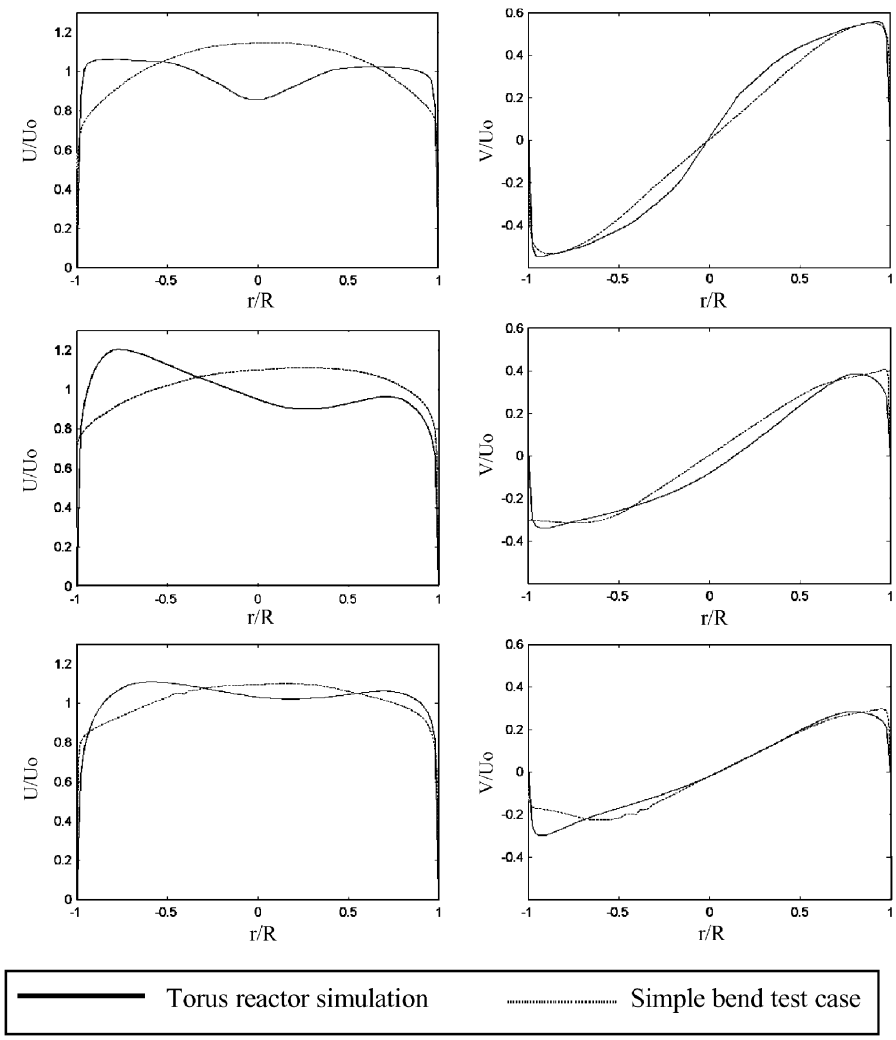


Fig. 8. Comparison of velocity profiles predicted in the first bend of the torus reactor with simple bend simulation with swirl flow at $Re = 35800$ (left: axial component; right: circumferential component; top: bend entry; middle: middle of the bend; bottom: bend outlet).

probe and a tracer technique, Khalid and Legrand (2001) observed experimentally the same over-velocity near the inner wall in the first bend next to the impeller. This confirms this feature as being specific of torus reactors.

This difference between the flow induced in the first bend of the torus reactor, and the one encountered in a simple 90° bend with swirl motion, is emphasized in Fig. 8, where simulated mean velocity profiles for axial and circumferential velocity components are presented for both cases at $Re = 35800$. Results of normalized velocity with respect to mean bulk velocity are presented for the inlet, the middle position and the outlet of corresponding bends. Normalized circumferential components appear similar in both cases, and only axial components are different, especially in the shape of the bend entry profile. For the single bend case, a fully turbulent developed pipe flow conditions was applied as inlet conditions, whereas, for the torus reactor case, the impeller involves two maxima of axial velocity near the walls. In the middle of the bend, the location of the maximum velocity is clearly different, in the outer part of the bend curvature for the single bend case, and in the inner part for the torus reactor case. As a consequence, the profile of axial component of velocity is axisymmetric in the outlet of the first bend for the torus reactor case, in opposite of the simple bend case where the bend curvature shift the maximum of axial velocity toward the outer part of the bend. This shows the effect of the impeller which generates specific downstream flow conditions. Due to the interaction with the radial pressure gradient generated by the first bend curvature, the resulting axial flow is mainly axisymmetric in the first bend outlet of the torus reactor and in the following straight part at position 1.

Next, in the second bend, a slight shift of the maximum of axial velocity in the inner part is also observed (Fig. 7). However, the flow in the following straight part is then characterized by a maximum velocity location in the outer part.

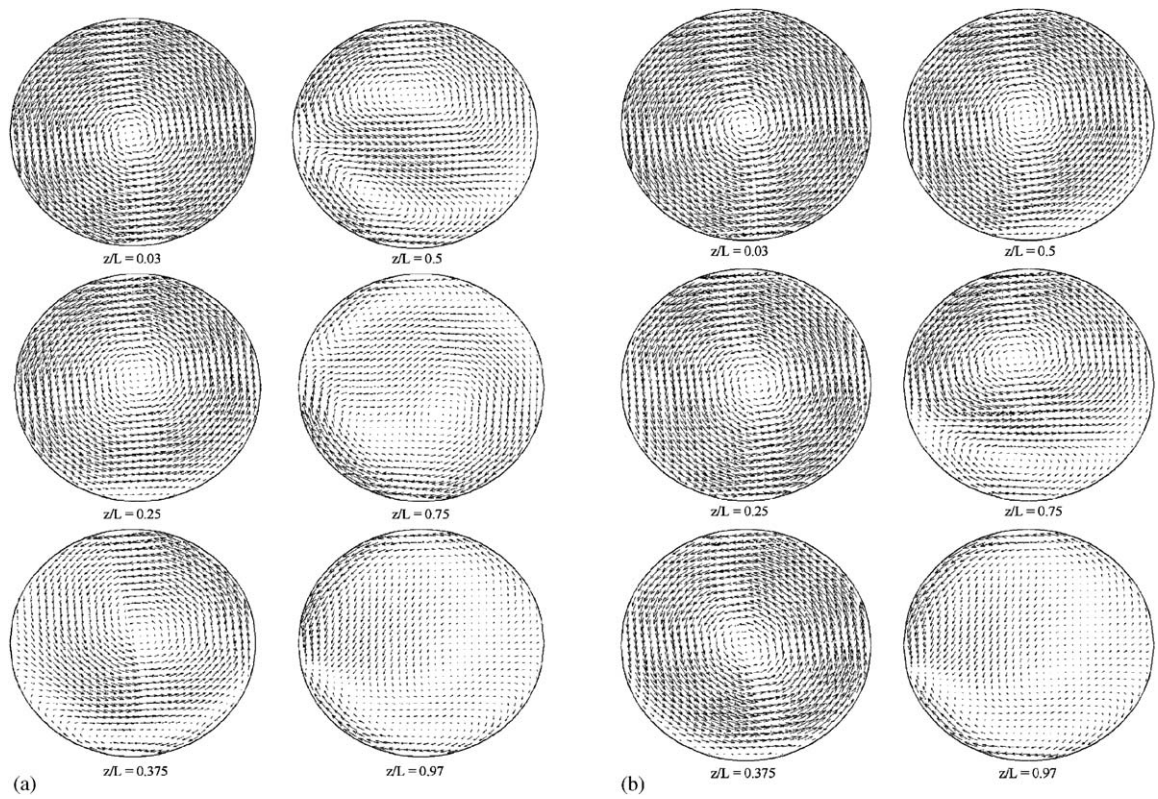


Fig. 9. Evolution of the flow structure in a pipe section: (a) for $N_3 = 500$ rpm; (b) for $N_2 = 1985$ rpm.

This shows the complex behavior of the flow in the torus reactor, and especially the relation between flow characteristics and the decay of the swirl motion when moving away from the impeller. Indeed, if circumferential velocities are analyzed, the swirl intensity can be considered as negligible after the second bend. The flow structure in the geometry can thus be roughly divided into two parts, the first ranged between the impeller and the second bend being highly driven by the motion involved by the impeller, that results in a reverse location of the maximum of axial velocity for example, and the second remaining part corresponding to more common flow conditions encountered in classical bends, with a location of this maximum in the outer part of the bend. Finally, it can be noticed that flow conditions at the outlet of the fourth bend, just upstream of the impeller, mainly exhibits axial motion with uniform profile. That emphasizes the influence of the impeller pumping effect. This feature again agrees with experimental observations of Khalid and Legrand (2001).

The complex evolution of flow conditions in the torus geometry is especially linked to the competition between centrifugal forces due to bends curvature and the swirling decaying motion. Both effects were especially discussed in Part I dealing with the simple bend test case. Without swirl motion, due to the imbalance between centrifugal force and radial pressure gradient, well-known instabilities of Dean-type appear in bends. When a swirl motion is added, those instabilities interact with the solid-body rotation involved by swirl, the resulting hydrodynamics depending on the swirl intensity applied in bend entry. For small intensity, a complex interaction between Dean vortices and swirl motion was observed, Dean vortices disappearing next in a sudden way for a higher intensity. For very high values of swirling intensities, the remaining flow is swirl-dominated, with only a poor influence of the bend curvature. So as to investigate this feature in the torus reactor case, the flow structure is represented by plotting velocity-fields in pipe sections for different axial distances from the impeller, for $N_2 = 1985$ rpm (Fig. 9a) and for a lower rotation speed of the impeller $N_3 = 500$ rpm (Fig. 9b). These results show that the solid-body rotation generated by the impeller is not observed up to the same distance for both impeller speeds, Dean-vortices appearing only in the third bend for $N_3 = 500$ rpm, whereas those structures are already observed in the second bend for $N_2 = 1985$ rpm. Despite higher values of circumferential velocities are naturally involved just downstream of the impeller for $N_2$, the resulting solid-body rotation vanishes more rapidly. This is again explained by the competition between bends and swirl effects. By increasing the rotational speed of the impeller, both swirl intensity and mean bulk velocity are increased. That results naturally in a greater initial solid-body rotation, but in counterpart, in more intensive centrifugal effects in bends. Because the initial swirl intensity and mean bulk velocity are different for both speeds of rotation of the

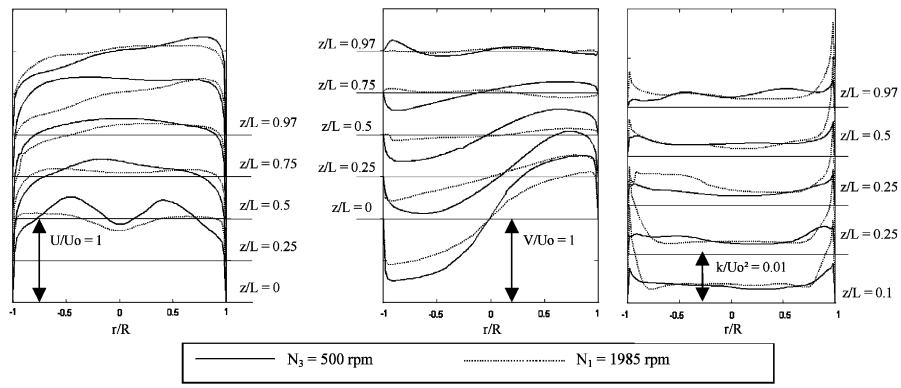


Fig. 10. Longitudinal evolution of predicted velocity profiles for $N_2 = 1985$ rpm and $N_3 = 500$ rpm (left: axial component; center: circumferential component; right: turbulent kinetic energy).

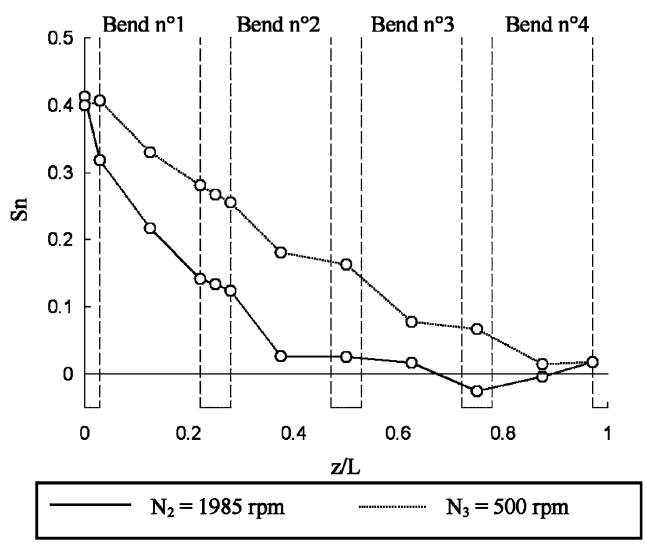


Fig. 11. Swirl number longitudinal evolution for $N_2 = 1985$ rpm and $N_3 = 500$ rpm.

impeller, the resulting flow is not the same. Normalized velocity and turbulent kinetic energy profiles obtained in straight parts are plotted in Fig. 10 for $N_2$ and $N_3$. A change in flow conditions is clearly observed when reaching the second straight part, with the shift of the maximum axial velocity towards the outer part of the reactor for the highest speed of impeller rotation, whereas an axisymmetric profile is still observed for the smaller value $N_3$. As shown by values of normalized circumferential velocities which are found to be negligible for $N_2$ after the second bend, this change in flow conditions corresponds to the disappearance of the rotating motion. Same conclusions are achieved when considering the turbulent kinetic energy. As already observed in part I, when the swirl motion is sufficiently intensive, turbulent kinetic energy profile tends to be axisymmetric, and bends effects are negligible. For low swirl intensity values, due to bend curvature, the maximum of turbulent kinetic energy is then shifted to the outer part of the reactor. This characterizes the evolution of the turbulent kinetic energy depicted in Fig. 10.

The swirl number $Sn$ is a good criterion to represent the competition between bend effects which are functions of the axial velocity, and the solid-body rotation generated by the swirl motion. This dimensionless parameter represents the axial flux of swirl momentum divided by the product of axial flux of axial momentum with the pipe diameter. Following the definition of Gupta et al. (1984), the swirl number $Sn$ is given by

$$Sn = \frac{\int_0^{D/2}\int_0^{2\pi} UVr^2\,\mathrm{d}r\,\mathrm{d}\theta}{D/2\int_0^{D/2}\int_0^{2\pi} U^2 r\,\mathrm{d}r\,\mathrm{d}\theta}, \tag{9}$$

where $U$, is the mean axial velocity component, $V$, the circumferential one, and $r$ and $\theta$ are radial and angular coordinates respectively, referred to pipe axis.

The influence of the swirl number on the resulting flow in bend outlet was established in part I, and it was concluded to a sudden modification of the flow with disappearance of Dean-vortices with the increase of the solid-body rotation, for a threshold value of $Sn$ applied in bend entry ranged between $Sn = 0.2$ and 0.3. Numerical simulation allows to calculate the evolution of the swirl number in the torus reactor, by numerically integrating profiles of axial and circumferential components of velocity-field following Eq. (9). Results are presented in Fig. 11.

The decrease of the swirl number with the distance from the impeller is clearly observed, starting from values of the same order of magnitude for both rotational impeller speeds, to be finally negligible at the end of the loop in the torus reactor. Effects of bends are shown too, with a faster decrease of $Sn$ when flowing through bends than in straight parts. This agrees with the simple bend test case, where the decrease of swirl intensity when crossing bend was found to be greater if initial values of the swirl number applied in entry were below the threshold value ranged between $Sn = 0.2$ and 0.3 (Part I, Fig. 11). In the case of torus reactor, such values of $Sn$ are encountered in almost all bend entries, except the first one. In all other bends, the solid-body rotation is thus in a more

or less intensive manner in competition with Dean vortices which tend to appear at those swirl intensities. Comparison with the velocity-fields obtained in pipe sections of the torus reactor (Fig. 8) confirms this hypothesis of Dean vortices appearance, when *Sn* decreases below the threshold value of *Sn* in bend inlet, which is found to be around 0.2 in this case. Considering the second bend, for $N_2 = 1985$ rpm, *Sn* value at bend inlet is around 0.12, and Dean vortices appear at the outlet. In contrary, for $N_3 = 500$ rpm, *Sn* value is around 0.25, and the solid-body rotation is still observed at the bend outlet.

Increasing the rotational speed of the impeller does not lead to a swirl flow persisting more longer in the geometry: the initial swirl is in fact more intensive, but as well as the bends centrifugal force. The resulting flow in the torus geometry is then a function of the balance between those two phenomena.

## 6. Conclusion

A numerical simulation was employed in this study to give complementary information to experimental characterization of flow in torus reactor. A commercial code was used for this purpose, and predictions using a $k$–$\omega$ model coupled with MRF simulation were validated with LDA measurements of mean velocity profiles.

The numerical tool was next used to investigate the particular behavior of flow in torus reactor, and especially its evolution along the distance from the marine impeller. Two major characteristics of the flow were emphasized. The first is linked to the particular motion involved by the impeller in the first downstream bend. Compared to classical bend pipe flows where the maximum of axial velocity is located in the outer part of the bend curvature due to the centrifugal force, this location is reversed in the inner part of torus reactor. The second feature is the competition between centrifugal forces and Dean vortices due to bends, with the solid-body rotation involved by the swirl flow generated by the impeller. Because of the swirl intensity decays with the distance from the impeller, competition between both phenomena evolves in the geometry. This evolution was found to be highly related to the swirl number *Sn*, and conclusions made in Part I with a simple bend test case were confirmed for the torus geometry. When the swirl number in a bend entry was found below a threshold value, the solid-body rotation cannot prevent from Dean vortices appearance in bends, and the swirl rotating motion is disturbed. The threshold value was found similar in both single bend and torus reactor simulation cases, namely $Sn \sim 0.2$, showing pertinence of this criterion to characterize the flow evolution in the torus reactor. This is explained by the double effect of the marine impeller that generates the axial flow motion, as well as the swirl one, both phenomena being considered in *Sn* definition. One main consequence is the faster decrease of swirl motion when increasing the impeller rotational speed. Only a half of the reactor length is submitted to a swirl flow for the highest impeller speed tested. By reducing the impeller speed, the swirl flow maintains farther away in the reactor.

In conclusion, the numerical tool appears as a promising way to investigate flow characteristics in torus reactor, and to better understand its running. The complex behavior is well represented, and essential information like evolution of the swirl motion, turbulent kinetic energy or Dean vortices appearance can be accessed. Such an approach will thus be very helpful in the optimization of such processes.

## Notation

| | |
|---|---|
| $d_1$ | impeller diameter, m |
| $d_2$ | impeller axis diameter, m |
| $D$ | pipe diameter, m |
| $F_g$ | geometrical parameter of the impeller |
| $k$ | turbulent kinetic energy, $m^2\,s^{-2}$ |
| $L$ | length of the torus reactor, m |
| $N$ | rotation velocity of the impeller, rpm |
| $p$ | pressure, Pa |
| $r$ | radial coordinate, m |
| $\vec{\mathbf{r}}$ | position vector in the rotating frame, m |
| $R$ | pipe radius, m |
| $R_c$ | bend curvature radius, m |
| $Sn$ | swirl number |
| $u_\tau$ | wall friction velocity, $m\,s^{-1}$ |
| $U$ | mean axial velocity component, $m\,s^{-1}$ |
| $U_0$ | mean bulk velocity, $m\,s^{-1}$ |
| $\vec{v}_r$ | relative velocity vector in the rotating frame, $m\,s^{-1}$ |
| $\vec{v}$ | absolute velocity vector, $m\,s^{-1}$ |
| $V$ | mean circumferential velocity component, $m\,s^{-1}$ |
| $y$ | wall distance, m |
| $y^+$ | wall distance in wall coordinate |
| $z$ | longitudinal coordinate, m |

*Greek letters*

| | |
|---|---|
| $\mu$ | dynamic viscosity of water, Pa s |
| $\rho$ | fluid density, $kg\,m^{-3}$ |
| $\bar{\tau}$ | molecular stress-tensor |
| $\bar{\tau}'$ | turbulent stress-tensor |
| $\phi$ | blade pitch of the impeller |
| $\Omega$ | angular velocity of the rotating frame, $rad\,s^{-1}$ |

## References


Anwer, M., So, R.M.C., 1993. Swirling turbulent flow through a curved pipe. Part I: effect of swirl and bend curvature. Experiments in Fluids 14, 85–96.

Bali, T., 1998. Modelling of heat transfer and fluid flow for decaying swirl flow in a circular pipe. International Communication in Heat and Mass Transfer 25 (3), 349–358.

Belleville, P., Nouri, L., Legrand, J., 1992. Mixing characteristics in the torus reactor. Chemical Engineering & Technology 15, 282–289.

Brucato, A., Ciofalo, M., Grisafi, F., Micale, G., 1998. Numerical prediction of flow-fields in baffled stirred vessels: a comparison of alternative modelling approaches. Chemical Engineering Science 53 (21), 3653–3684.

Gupta, A.K., Lilley, D.G., Syred, N., 1984. Swirl Flows.. Abacus Press, Cambridge.

Harris, C.K., Roekaerts, D., Rosendal, F.J.J., 1996. Computational fluid dynamics for chemical reactor engineering. Chemical Engineering Science 51 (10), 1569–1594.

Khalid, A., Legrand, J., 2001. Energy dissipation distribution and mixing in a torus reactor. Chemical Engineering Communications 185, 141–164.

Khalid, A., Legrand, J., Rosant, J.M., 1996. Turbulent flow induced by an impeller in a closed toroidal loop. Journal of Fluids Engineering 118, 677–684.

Legrand, J., Belleville, P., 2002. Flow characteristics and transport phenomena in toroidal loop reactors. Chemical Engineering Technology 25 (6), 667–670.

Legrand, J., Guéguen, J., Berot, S., Popineau, Y., Nouri, L., 1997. Acetylation of pea isolate in a torus microreactor. Biotechnology and Bioengineering 53 (4), 410–414.

Montane, G., Lee, K.C., Brucato, A., Yianneskis, M., 2001. Numerical simulations of flow pattern on impeller clearance in stirred vessels. Chemical Engineering Science 56, 3751–3770.

Nouri, L., Legrand, J., Popineau, Y., Belleville, P., 1997. Enzymatic hydrolysis of wheat proteins. Part II . Comparison of performance of batch-stirred and torus reactors. Chemical Engineering Journal 65, 195–199.

Pericleous, K.A., Patel, M.K., 1987. The modelling of tangential and axial agitators in chemical reactors. Physico Chemical Hydrodynamics 8 (2), 105–123.

Revstedt, J., Fuchs, L., Trägardh, C., 1998. Large eddy simulation of the turbulent flow in a stirred reactor. Chemical Engineering Science 53 (24), 4041–4053.

Sato, Y., Murakami, Y., Hirose, T., Hashigushi, Y., Ono, S., Ichikawa, M., 1979. Flow pattern, circulation velocity and pressure loss in loop reactor. Journal of Chemical Engineering of Japan 12, 448–453.

Sudo, K., Sumida, M., Hibara, H., 1998. Experimental investigation on turbulent flow in a circular-sectioned 90-degrees bend. Experiments in Fluids 25, 42–49.

Tanaka, M., O'Shima, E., 1988. Dispersing behavior of droplets in suspension polymerization of styrene in a loop reactor. Canadian Journal of Chemical Engineering 66, 29–35.

Ten Cate, A., Dersksen, J.J., Kramer, H.J.M., Van Rosmalen, G.M., Van den Akker, H.E.A., 2001. The microscopic modelling of hydrodynamics in industrial crystallizers. Chemical Engineering Science 56, 2495–2509.

Wilcox, D.C., 1998. Turbulence Modelling for CFD. DCW Industries. La Canada, California.

Yoon, H.S., Sharp, K.V., Hill, D.F., Adrian, R.J., Balachandar, S., Ha, M.Y., Kar, K., 2001. Integrated experimental and computational approach to simulation of flow in a stirred tank. Chemical Engineering Science 56, 6635–6649.